

# Quantification of pulsed saturation transfer at 1.5T and 3T

Rachel W. Chan<sup>1</sup>  | Sten Myrehaug<sup>2,3</sup> | Greg J. Stanisz<sup>1,4,5</sup> | Arjun Sahgal<sup>1,2,3</sup> | Angus Z. Lau<sup>1,4</sup>

<sup>1</sup>Department of Physical Sciences, Sunnybrook Research Institute, Toronto, Canada

<sup>2</sup>Department of Radiation Oncology, Sunnybrook Health Sciences Centre, Toronto, Canada

<sup>3</sup>Department of Radiation Oncology, University of Toronto, Toronto, Canada

<sup>4</sup>Department of Medical Biophysics, University of Toronto, Toronto, Canada

<sup>5</sup>Department of Neurosurgery and Pediatric Neurosurgery, Medical University, Lublin, Poland

## Correspondence

Rachel W. Chan, 2075 Bayview Ave,  
Toronto, Ontario, M4N 3M5, Canada.  
Email: rchan@sri.utoronto.ca

## Funding information

NSERC, Grant/Award Numbers:  
RGPIN-2017-06596; NSERC, Grant/Award  
Numbers: CRDPJ 507521-16; Terry Fox  
(New Frontiers Program Project Grant); CIHR

**Purpose:** To compare magnetization transfer (MT) and CEST effects between 1.5T and 3T in phantom and in vivo experiments.

**Methods:** A pulsed saturation scheme using block-shaped pulses separated by gaps was used to overcome the single RF amplifier duty cycle limitations of a clinical 1.5T scanner. Modeling was performed by incorporating the extended phase graph formalism into a Bloch-McConnell simulation. Two saturation pulse types (with long and short pulses) were used. Estimated parameters for MT (the semi-solid pool fraction,  $M_0^B$ ; the semi-solid transverse relaxation time,  $T_2^B$ ) and CEST (asymmetry; areas) were compared between 1.5T and 3T in phantoms and in the healthy brain.

**Results:** Improved fits were shown after inclusion of extended phase graphs. Semi-solid pool fractions in phantom (for agar with ammonium chloride) were higher for short compared to long pulses at 3T (by 19% over all concentrations) and higher at 1.5T compared to 3T (by 5%) using short pulses. In the in vivo experiments, differentiation of white and gray matter was seen in the brain at both field strengths with improved white–gray matter contrast at 3T. In white matter, the mean semi-solid fractions were  $18 \pm 2\%$  at 3T and  $15 \pm 2\%$  at 1.5T. The CEST asymmetry in white matter was negative ( $-4.9 \pm 0.4\%$ ) at 3T and zero ( $0.0 \pm 0.3\%$ ) at 1.5T.

**Conclusions:** The pulsed saturation method with short pulses, using the extended phase graph formalism in the Bloch McConnell simulations, led to improved model fits to the data, when compared to those without extended phase graphs.

## KEYWORDS

chemical exchange saturation transfer, extended phase graphs, magnetization transfer, pulsed saturation, quantitative imaging

## 1 | INTRODUCTION

Saturation transfer MRI techniques include quantitative magnetization transfer (qMT)<sup>1,2</sup> and CEST.<sup>3</sup> In particular, CEST

has gained much interest in recent years, providing a novel contrast mechanism in MRI.<sup>4–6</sup> Many of the current CEST techniques focus on amide proton transfer (APT),<sup>7–16</sup> in which amides contribute to the CEST signal at around 3.5 ppm. APT

CEST has shown potential for predicting histopathological grade (15) and distinguishing pseudoprogression from true progression.<sup>10</sup> In addition, at 3T, CEST and qMT have demonstrated the ability to predict response to chemoradiation in human glioblastoma (GBM).<sup>11,17</sup> Regnery et al.<sup>16</sup> also reported CEST MRI as an imaging modality predicting early progression in GBM although at 7T. Furthermore, 7T glioma CEST studies<sup>18-21</sup> have reported unique image contrast,<sup>19</sup> with ability to predict mutation status<sup>21</sup> and yield additional information on peritumoral hyperintensities.<sup>20</sup> Desmond et al.<sup>22</sup> showed, with 3T CEST in patients with brain metastases, that the nuclear Overhauser effect (NOE) peak amplitude can predict volume changes after treatment and predict response. At present, CEST metrics, including APT and NOE, continue to show promise as alternative contrast mechanisms in various brain cancer applications.

The majority of CEST studies have been conducted at field strengths of 3T or higher. Higher field strengths provide increased separation of CEST peaks (minimizing the effect of direct saturation near the water peak) and higher SNR. The applicability of this methodology at lower field strength, such as at 1.5T, remains a question. The aims of this study were to quantify the effects of CEST at 1.5T in phantoms and in the healthy brain and compare them to those obtained at 3T.

In the present work, several technical advances were required to enable quantitative saturation transfer MRI at 1.5T on a typical MR scanner. Although continuous wave RF irradiation (with durations of at least 5 times the  $T_1$  relaxation time) can be used in preclinical scanners to achieve steady-state saturation, hardware limitations on clinical systems require pulsed saturation transfer schemes<sup>23-25</sup> where the saturation module consists of trains of RF pulses separated by gaps.<sup>26-28</sup> The maximum duration of individual RF pulses may range from  $<20$  ms<sup>23,29</sup> to  $>100$  ms<sup>17,25,30,31</sup> depending on the amplitude and duty cycle limits of the RF amplifier. Gaussian or sinc pulses are typically used but require an approximation in the model where the shaped pulse needs to be divided into segments on the order of microseconds. For simplicity, block (rectangular shaped) pulses were used in our study. Although the short and repetitive block pulses have oscillations present in the frequency profile, we demonstrated that accurate results could be obtained by fitting the spectra to the Bloch-McConnell (BM) equations using exact RF amplitudes and timings.<sup>23,29</sup> As in previous literature, modeling of pulsed saturation used numerical solutions of the time-dependent Bloch equations,<sup>23</sup> because analytic solutions for continuous wave steady-state saturation are not valid for pulsed saturation transfer schemes. Recently, Malik et al.<sup>32</sup> used the extended phase graph (EPG) framework<sup>33,34</sup> for the modeling of multicompartamental systems with exchange, called “EPG-X.” In EPG-X, the effects of RF excitation were separated from those of relaxation and exchange. Our implementation builds on

EPG-X and is a more general approach that combines the effects of RF with relaxation and exchange. In this work, our modified EPG framework was applied to model the effect of closely spaced RF pulses with multiple gradient spoilers within the saturation module.

Using the aforementioned techniques, CEST and qMT parameters were quantified at 1.5T using a pulsed saturation scheme that consisted of short, block pulses. The main purpose of the study was to compare the MT and CEST effects between 1.5T and 3T. For in vivo comparison, the brain of the same healthy subject was scanned at both field strengths. For phantom comparison, the same phantom containing various concentrations of ammonium chloride ( $\text{NH}_4\text{Cl}$ ) was scanned at 1.5T and 3T. In the absence of steady-state saturation, pulse type L, used for both MT and CEST saturation, was considered the gold standard for accuracy. Because the 1.5T scanner necessitated the use of short pulses (whereas previous MT and CEST studies at 3T were performed with long pulses),<sup>11,17</sup> extra experiments were performed on the 3T scanner with both short and long pulses implemented for comparison.

## 2 | METHODS

### 2.1 | MR experiments

#### 2.1.1 | Phantom experiments at 1.5T

MR imaging was conducted at 1.5T (Ingenia, Philips Medical Systems, Best, the Netherlands) using a 16-channel head coil. The phantom consisted of samples with varying  $\text{NH}_4\text{Cl}$  concentrations (0 M, 0.25 M, 0.5 M, and 1.0 M) with CEST contributions at the amine frequency offset ( $\sim 2.3$  ppm). Each sample was mixed with 2% agar to mimic the MT pool. The RF irradiation of the clinical 1.5T scanner had sub-pulse durations that were limited to  $\sim 10$  ms and required gaps to be inserted in the saturation module, reducing the short-term duty cycle. A pulsed saturation scheme (called pulse type “S” for “short”) was used that consisted of 10 ms block pulses for MT and 0.5 ms pulses for CEST, both separated by short gaps in time. A diagram is shown in Figure 1A for MT and CEST saturation with pulse type S.

#### 2.1.2 | Comparison of saturation pulse types L and S at 3T

At 3T (Achieva, Philips Medical Systems), 2 saturation schemes, (1) pulse type S (similar to that at 1.5T), and (2) a pulsed scheme with individual elements with longer durations ( $>200$  ms) (called pulse type “L” for “long”, as used by Mehrabian et al.<sup>17</sup> shown in Figure 1B) were compared. The 3T system allowed both (L and S) pulse types

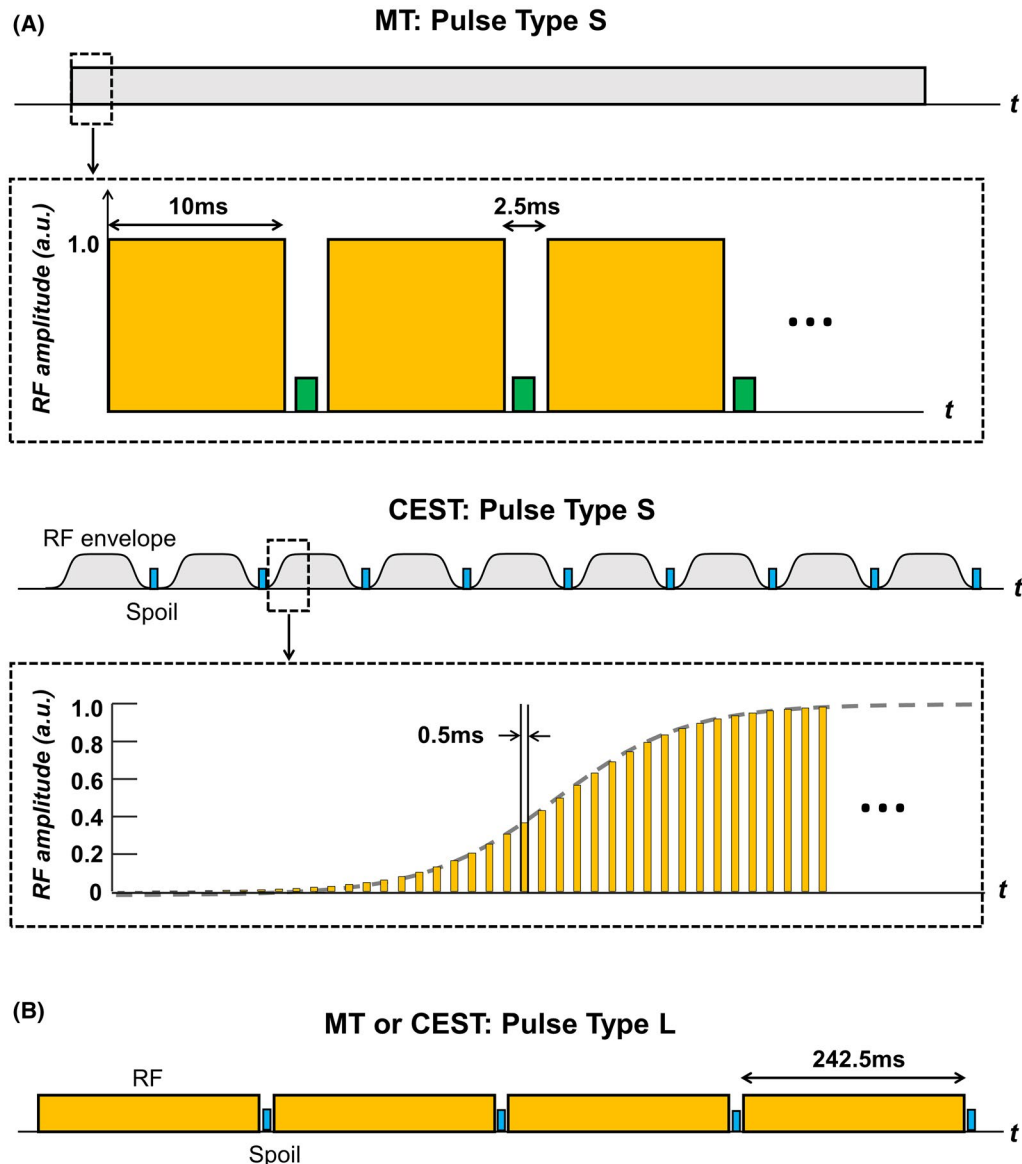


**FIGURE 1** Pulsed saturation modules. Two saturation pulse types (“S” for short and “L” for long) are illustrated for the MT and CEST sequences. (A) For the MT saturation, pulse type S consisted of a series of 10-ms block pulses separated by 2.5-ms gaps with gradient spoilers. For the 3T experiments, 20-ms block pulses were used in several of the MT scans. For CEST, pulse type S consisted of 9 repetitions of Fermi pulses, with gradient spoiling in between the Fermi repetitions. Each Fermi pulse consisted of short 0.5-ms RF blocks separated by 0.5-ms gaps. (B) Pulse type L for the MT and CEST sequences consisted of block pulses, each with a duration of 242.5 ms and separated by gaps with spoilers. The 4 pulse version is shown in this figure. For MT, either 2 or 4 block pulses were used. For CEST, 4 block pulses were used. Both pulse types (L and S) were implemented on the 3T scanner. The 1.5T scanner allowed only pulse type S to be implemented

to be implemented. Images at 3T were obtained using an 8-channel head coil.

### 2.1.3 | Experiments in the healthy brain at 1.5T and 3T

Experiments were performed in the same healthy volunteer to compare in vivo MT and CEST parameters at 1.5T using pulse type S and at 3T using pulse type L. The study was approved by the institutional research ethics board at Sunnybrook Health Sciences Centre, and informed consent was obtained.

## 2.2 | MR imaging protocol

### 2.2.1 | Saturation sequences

For pulse type L, both MT and CEST saturation pulses consisted of block pulses (each having relatively long durations of 242.5 ms), as in previous work<sup>11,17</sup> (Figure 1B). In the MT experiments with pulse type L, sets of either 2 or 4 blocks were used for saturation and, in the CEST experiments with pulse type L, 4 consecutive blocks were used. In the MT experiments for pulse type S, the saturation module consisted of

short repetitive blocks of RF having durations of 10 ms (or 20 ms, in 1 of the 3T scans) separated by 2.5-ms gaps (Figure 1A). In the CEST experiment with pulse type S, the saturation module consisted of block pulses of 0.5 ms separated by 0.5-ms gaps and modulated by a Fermi pulse envelope (Figure 1A), with the Fermi pulses repeated 9 times to generate increased saturation. Compared to pulse type S, pulse type L was more similar to a steady-state saturation scheme, but was not strictly steady state because the saturation duration was shorter than  $5 \times T_1$ .

Using pulse type S, the frequency profiles were oscillatory and needed to be different for the MT and CEST spectra. A short pulse duration of 0.5 ms was chosen for the CEST sequence to allow for a broader frequency range that covers the CEST  $z$ -spectrum (so that repetitions in the frequency profile occur outside of this range). Hardware constraints required there to be gaps with a minimum of 0.5-ms duration for the  $B_1$  amplitudes used. This gap was kept at its minimum (i.e., 0.5 ms) so that the overall saturation efficiency was not compromised. Spoilers were used after each of the 9 Fermi pulses (with each Fermi pulse envelope consisting of 125 repetitions of 0.5 ms pulses with 0.5 ms gaps). At 1.5T, 12 ppm corresponds to a range of 766 Hz and the replicas caused by these 1 ms (0.5 ms on/0.5 ms off) repetitions occurred outside of the central 1 kHz range. For the MT sequence, it was not possible to avoid signal oscillations within the MT spectrum. Therefore, longer pulses of 10 ms were used at 1.5T to increase saturation efficiency. This was the maximum pulse duration allowed by the hardware for the  $B_1$  amplitudes used. The gap durations of 2.5 ms used in the MT sequence allowed spoiling gradients to be inserted between every pulse.

Supporting Information Table S1 in shows the MR protocol for the MT and CEST sequences used in phantom experiments. Multiple RF irradiation powers were used for both the MT and CEST experiments. In the MT phantom experiments where pulse scheme S was used for saturation, there were additional frequency offsets (between 1510–1690 Hz in steps of 10 Hz at 1.5T and 1550–1650 Hz in steps of 5 Hz at 3T).

The in vivo experiments consisted of different sets of saturation parameters from those of the phantom experiments. Supporting Information Table S2 shows the in vivo MR protocol for the MT and CEST sequences. Because of time constraints, the frequency offsets in the in vivo MT scans were not sampled as finely compared to phantom experiments (with pulse type S) where some frequency offsets were sampled every 10 Hz (at 1.5T) or 5 Hz (at 3T). The sets of  $B_1$  amplitudes used in the in vivo scans for CEST were  $B_{1,RMS} \approx \frac{1}{2} \times B_{1,max} = \frac{1}{2} \times \{2.05, 4.1\} \mu\text{T}$  at 1.5T, and  $B_{1,RMS} = \{0.52, 0.52, 0.75\} \mu\text{T}$  at 3T.

### 2.2.2 | $T_1/T_2/B_1/B_0$ mapping sequences

To perform quantitative CEST and MT analysis, additional sequences were required to assess sample relaxation and  $B_0$

and  $B_1$  inhomogeneities. The water shift and  $B_1$  (WASABI) sequence<sup>35</sup> was used for simultaneous pixelwise estimation of  $B_1$  scaling and  $B_0$  frequency shift. It consisted of a 5-ms block pulse and  $B_1$  amplitude of 3.6  $\mu\text{T}$ . The frequency offsets were stepped in forward and in reverse order, and the 2 signals were averaged. A spoiled gradient echo sequence was used for the WASABI sequence. The readout module and acquired voxel size were kept the same as the MT and CEST sequences. A spoiled gradient echo sequence was used for  $T_1$  mapping and acquired with multiple flip angles ( $2^\circ$ ,  $5^\circ$ ,  $10^\circ$ ,  $15^\circ$ ,  $20^\circ$ ,  $25^\circ$ , and  $30^\circ$ ). The estimated  $B_1$  from the WASABI sequence was used in the estimation of the observed  $T_1$ ,  $T_1^{OBS}$ , in addition to MT and CEST parameter quantification.  $T_2$  mapping was performed with a  $T_2$ -weighted multi-echo sequence to obtain an observed  $T_2$ , which was used as an initial value for subsequent estimation of the  $T_2$  of the water pool,  $T_2^A$ . Phantom experiments were performed at a room temperature of 21°C. Parameters used in the phantom experiments are listed in Supporting Information Table S3. In the in vivo experiments, anatomic 3D  $T_1$ -weighted images and  $T_2$ -weighted fluid-attenuated inversion recovery (FLAIR) images were also acquired.

## 2.3 | Image processing

For the in vivo scans, the  $T_1$ -weighted and  $T_2$ -weighted FLAIR volumes were first registered using the “flirt” function from FSL (FMRIB, Oxford, UK; <http://www.fmrib.ox.ac.uk/fsl>). From each of the 3D ( $T_1$ -weighted and  $T_2$  FLAIR) volumes, slices were extracted that corresponded to the scanned CEST or MT slice. For the CEST scans, motion correction was performed across the saturation frequency offsets using the FSL “mcflirt” function before parameter estimation.

## 2.4 | Parameter quantification

Both region-of-interest and pixelwise fitting were performed for phantom and in vivo scans. MT and CEST parameters were quantified. The MT and CEST parameter values were compared in white matter regions on both 1.5T and 3T scans.

### 2.4.1 | $B_0$ and $B_1$ estimation

Detailed steps in the processing pipeline for quantifying the MT and CEST parameters are illustrated in the flowchart of Figure 2. In step 1, the pixelwise  $B_0$  and  $B_1$  values were estimated from the WASABI sequence.<sup>35</sup> Similar to water saturation shift referencing (WASSR),<sup>36</sup> the WASABI sequence uses off-resonant, low-power RF pulses to estimate the water-frequency-shift,  $B_0$ . Unlike the WASSR method, the WASABI method simultaneously maps both the  $B_0$

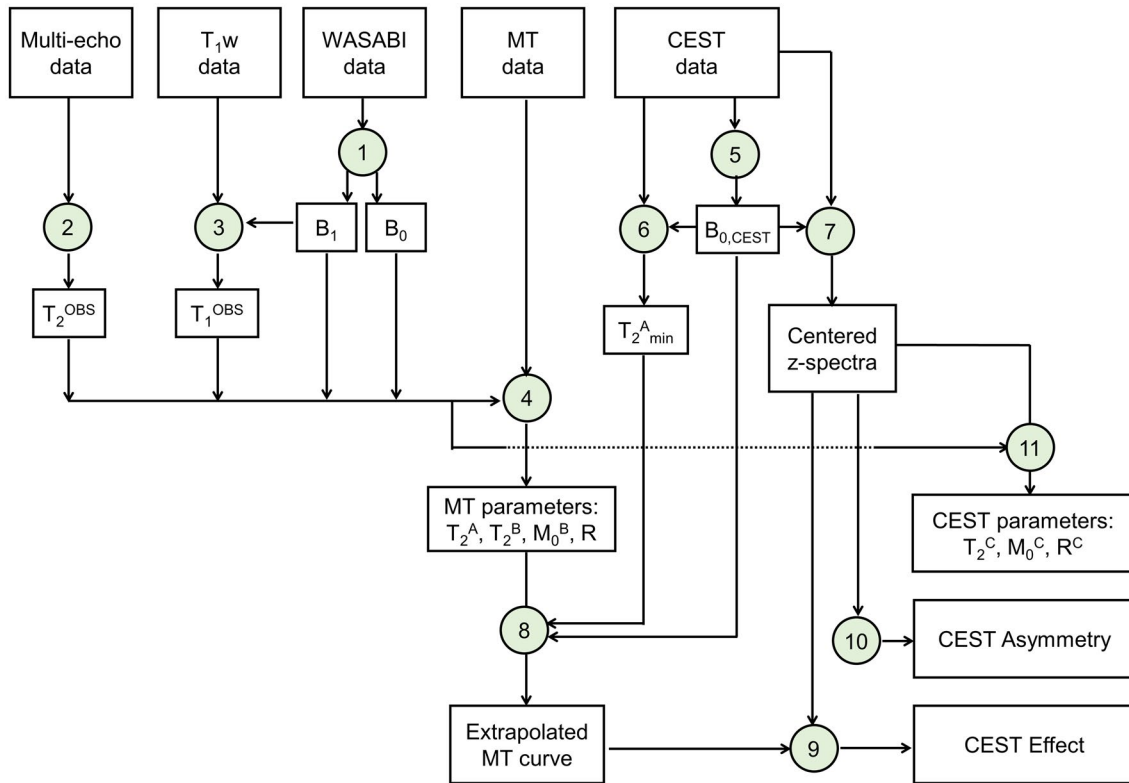


**FIGURE 2** Processing pipeline for MT and CEST parameter quantification. Input and output data are represented by rectangles. Computational steps are represented by numbered circles. The steps are: (1)  $B_0$  and  $B_1$  mapping using WASABI data, (2)  $T_2$  mapping to obtain the observed  $T_2$  estimate ( $T_2^{\text{OBS}}$ ), (3)  $T_1$  mapping to obtain the observed  $T_1$  estimate, ( $T_1^{\text{OBS}}$ ), (4) quantitative MT parameter estimation, (5) frequency offset determination for CEST, (6) determination of the  $T_2^A$  constraint based on CEST data, (7) centering of the z-spectra by  $B_{0,C}$ , (8) extrapolation of the quantitative MT signal to CEST frequency offsets, (9) CEST effect quantification, (10) CEST asymmetry quantification, and (11) quantitative modeling of CEST parameters

frequency shift and the  $B_1$  scale. Accurate  $B_1$  information is important for the estimation of  $T_1$  and for MT and CEST quantification. In the WASABI sequence, the  $B_0$  is encoded in the shift of the symmetry axis and the  $B_1$  is encoded in the periodicity of the sinc-like spectrum. The  $B_1$  and  $B_0$  was estimated by fitting WASABI spectrum to an analytic model provided by Scheunke et al.<sup>35</sup>

#### 2.4.2 | Estimation of the observed $T_1$ , $T_2$

The observed  $T_1$  and  $T_2$  were also used for the MT fits. The observed  $T_2$  relaxation time ( $T_2^{\text{OBS}}$ ) was estimated from a set of multi-echo spin echo data acquired at various TE (Figure 2, step 2). The observed  $T_1$  relaxation time ( $T_1^{\text{OBS}}$ ) was estimated using the variable flip angle (VFA) method.<sup>37</sup> The inversion recovery sequence is considered to be the gold standard for measuring  $T_1^{\text{OBS}}$ . It has been shown that the observed  $T_1$  from VFA fitting is a more complex function of the signal behavior as a result of saturation and, as such, the inversion recovery and VFA measures of  $T_1^{\text{OBS}}$  are not equivalent.<sup>38</sup> However, the scan durations of inversion recovery are long compared to the VFA method. This is especially true

for 3D imaging and, therefore, the VFA method was chosen for this study. The VFA method is known to be influenced by  $B_1$  inhomogeneity, which causes the actual flip angle to deviate from the nominal flip angle. Here, the flip angle deviations were taken into account by scaling the nominal flip angle based on the  $B_1$  value (estimated from the WASABI sequence as in step 3 of Figure 2) in the  $T_1$  fitting procedure to estimate the  $T_1^{\text{OBS}}$  value. The set of nominal flip angles used in the VFA method were  $\{2,5,10,15,20,25,30\}^\circ$  with  $TR/TE = 10/4.6$  ms.

#### 2.4.3 | MT and CEST parameter estimation

The MT data were fitted using a 2-pool qMT model<sup>2</sup> consisting of a liquid bulk water pool (“A”) and semi-solid MT pool (“B”) (Figure 2, step 4). Experimental data were fitted to the BM equations to model exchange between the 2 pools. Free parameters of the qMT estimation included the  $T_2$  of the liquid pool ( $T_2^A$ ), which was allowed to vary from the observed  $T_2$  (i.e., the  $T_2$  map value), the equilibrium magnetization fraction of the semi-solid pool ( $M_0^B$ ) relative to water, the  $T_2$  relaxation time of the semi-solid pool ( $T_2^B$ ), and the exchange

rate of magnetization between the water and semi-solid pools (R). The Bloch equations were solved numerically by incorporating the scan parameters listed in Supporting Information Tables S1, S2, and S3. A Gaussian lineshape<sup>2</sup> for the semi-solid pool was used in phantom experiments with agar, and a Super-Lorentzian lineshape<sup>39</sup> was used in the brain. As in Portnoy and Stanis,<sup>25</sup> the magnetization was propagated through each time interval, with the endpoint values used as initial conditions for the next interval. The pulse sequence was divided into intervals that had constant RF amplitudes for the duration of each interval. Propagation of the magnetization was performed for all intervals in the pulse sequence including the saturation and readout modules, and any delay periods to account for  $T_1$  and  $T_2$  relaxation. As the magnetization from the previous shot-to-shot interval could affect the signal of the next one, the shot-to-shot intervals and saturation frequency offset order were taken into account. For the readout module, the TR, TE, and (variable) flip angles of the spoiled gradient echo sequence were included. The fitted  $T_1$  of the free water pool, or  $T_1^A$ , was distinct from the  $T_1^{\text{OBS}}$  estimate. The  $T_1^{\text{OBS}}$  value, previously estimated from the VFA and WASABI sequences, was used as an initial guess for  $T_1^A$  in the estimation of the MT parameters.  $T_1^A$  was a variable parameter and its value was computed at each step of the objective function minimization (as a function of  $T_1^{\text{OBS}}$  and other MT parameters including  $T_1^B$ ,  $M_0^B$ , and R) according to Henkelman et al.<sup>2</sup> The value of  $T_1^B$  was fixed to 1 s as in previous work.<sup>2,17,30</sup> The data points acquired at the 3 most negative MT frequency offsets were excluded from all fits.

For both MT and CEST sequences, the extended phase graphs (EPG) method was incorporated in the BM simulation model. In the present work, there were multiple spoiling gradients within the saturation modules. In the CEST saturation module, there were 9 spoiling gradients (between the Fermi pulses) and in the saturation module of the MT experiments, there were up to 90 spoiling gradients (during the 2.5-ms gaps). Repetitive RF pulses with interleaved spoiling caused signal in higher order EPG configuration states to be generated that were then refocused by subsequent pulses. Therefore, it was important for the simulations of exchange to include these higher order echo contributions for improved accuracy. To keep track of magnetization in higher order echoes, EPG was implemented both for the saturation and variable-flip-angle readout modules. EPG theory used in the present work is summarized in the Appendix. The EPG method used in our work is different from that described in the EPG-X approach.<sup>32</sup> In Malik et al.,<sup>32</sup> the effects of RF excitation are separated from relaxation and exchange. In our study, matrix A (in the Appendix) combines the effects of RF with relaxation and exchange. This is a more general approach, which was useful for modeling the pulsed saturation scheme used in our study. Our EPG implementation was used to account for multiple spoilers within the saturation module.

Specifically, to model the saturation pulses, the amplitudes and durations of each segment were successively inputted into the Bloch simulation. If the segment were a gap, then an amplitude of zero was included. If there were spoiler gradients during the gaps, that was taken into account by incrementing the EPG configuration state. All numerical simulations were processed using MATLAB (version 2016b, 9.1.0.441655; The MathWorks, Natick, MA). The BM equations were fitted in MATLAB using the optimization function *lsqnonlin*. The 68% confidence intervals were computed based on Equation B1 in the work by Desmond and Stanis.<sup>30</sup>

In phantom experiments, a 3-pool (water/MT/CEST) model was used to estimate physical CEST parameters for 1.0 M  $\text{NH}_4\text{Cl}$  with 2% agar. Quantitative CEST parameters derived from this approach would directly be comparable across scanners. However, estimating reliable parameters using a 3-pool model would be difficult in vivo at 1.5T because of small CEST contributions. As such, the 3-pool fitting method was used only in phantom experiments (with relatively high solute concentrations). The aim was to establish congruence between pulse types L and S. The reason for validating pulse type S was for implementation on the 1.5T scanner. Three-pool fitting was performed for both field strengths (1.5T and 3T) and for both pulse types (long and short). The  $T_2$  of the CEST pool ( $T_2^C$ ), the equilibrium magnetization of the CEST pool ( $M_0^C$ ), and the exchange rate between the water and CEST pools ( $R^C$ ) were fitted. The  $T_1$  of the CEST pool ( $T_1^C$ ), was set to 1 s. The  $T_2$  of the water pool ( $T_2^A$ ) was a free parameter in the 3-pool fits. The MT parameters ( $T_2^B$ ,  $M_0^B$ , and R) were also free parameters in the 3-pool fit, with values initialized to those estimated using the MT data set. Similar to the 2-pool fits, the 3-pool model was also based on EPG.

#### 2.4.4 | MT extrapolation

For in vivo experiments, the CEST pool was not directly fitted to the z-spectrum (i.e., a 3-pool model was not used) because of the low in vivo CEST effect compared to that of 1.0 M  $\text{NH}_4\text{Cl}$  in phantoms. Instead, to quantify the CEST effect, Z-spectra were first extrapolated from the qMT parameters.<sup>40</sup> In Heo et al.,<sup>40</sup> this was known as the extrapolated semi-solid MT reference or “EMR” signal, which had effects of semi-solid MT pool but not those of CEST. Specifically, the fitted MT parameters ( $T_2^A$ ,  $T_2^B$ ,  $M_0^B$ , and R) were forward-propagated through the BM model using sequence parameters and frequency offsets of the CEST scans. For the extrapolation of qMT parameters onto CEST frequency offsets, the MT parameters ( $T_2^B$ ,  $M_0^B$ , R) were kept fixed to previously fitted values. From the CEST data, the  $T_2$  relaxation time of the liquid pool ( $T_2^A$ ) was estimated from the CEST data before extrapolation.  $T_2^A$  was fitted to the CEST data from each RF amplitude, resulting in multiple estimated  $T_2^A$  values. Then, the minimum value,  $T_2^{\text{A min}}$ , was used as the constraint (Figure 2,

step 6) to generate the extrapolated MT curve. Choosing the minimum  $T_2^A$  (that corresponds to a broader z-spectrum around the water peak) maximally constrains the extrapolated MT curve to ensure that it does not exceed the signal of the CEST z-spectra. The extrapolation was performed for both phantom and in vivo experiments on a pixelwise basis.

### 2.4.5 | CEST effect and asymmetry

For both phantom and in vivo experiments, the CEST effect based on amide, amine, and NOE was computed (Figure 2, step 9) as the difference between the extrapolated MT curve (i.e., the output from step 8 in Figure 2) and the CEST z-spectra after it was centered in the frequency offset direction by  $B_0$  correction (i.e., the output from step 7 in Figure 2). The advantage of this subtraction approach is that it can be used to measure the CEST effect even at low solute concentrations where estimating reliable parameters from 3-pool modeling would be difficult. This approach required only the MT effects to be modeled quantitatively (to obtain the MT-extrapolated curve for the subtraction).

The CEST asymmetry was also computed (Figure 2, step 10) and quantified as

$$\text{CEST}_{\text{asym}} = \frac{S(-\Delta) - S(\Delta)}{S_0}$$

where  $S$  is the z-spectrum signal,  $S_0$  is the reference signal far off resonance assumed to be without MT or CEST effects.<sup>30</sup> For  $S(\Delta)$ , the signal was averaged between 2–3 ppm (around the ammonium chloride amine peak ~2.3 ppm) in phantom experiments and averaged between 3–4 ppm in the brain (around the amide peak ~3.5 ppm).

For phantom experiments, the CEST effect and asymmetry were compared at the  $B_1$  amplitudes that generated the maximum CEST effect (i.e., at  $B_1 = 1.0 \mu\text{T}$  for pulse type L at 3T,  $B_{1,\text{RMS}} \approx \frac{1}{2} \times B_{1,\text{max}} = 1.0 \mu\text{T}$  for pulse type S at 3T, and  $B_{1,\text{RMS}} = 0.5 \mu\text{T}$  for pulse type S at 1.5T). In the healthy brain, the CEST effect (of both amide and NOE) and asymmetry were computed for  $B_{1,\text{RMS}} = 1.5 \mu\text{T}$  at 1.5T (interpolated from the nominal  $B_{1,\text{RMS}}$  amplitudes of 1.0  $\mu\text{T}$  and 2.05  $\mu\text{T}$  after pixelwise correction for  $B_1$  inhomogeneity), and  $B_{1,\text{RMS}} = 0.6 \mu\text{T}$  at 3T (interpolated from the nominal  $B_{1,\text{RMS}}$  of 0.52  $\mu\text{T}$  and 0.75  $\mu\text{T}$ ). The CEST asymmetry does not require quantitative modeling and would be applicable at any solute concentration. Unlike CEST asymmetry, the CEST effect quantity can be used to separate the amide and NOE effects.

## 3 | RESULTS

Figure 3A displays examples of the MT fitted curves overlaid on the acquired data for the phantom experiment at

1.5T (using pulse type S). The MT curves are well fitted to the data points, including at the oscillations present in the spectra (Figure 3A, box 1). In box 2 of Figure 3A, the signal oscillations are shown in the zoomed-in plots over the region where more measurements were acquired. The oscillatory signal was because of the frequency response of the short repetitive pulses used for saturation. The model was not shifted in the frequency offset direction with respect to the data points indicating that the estimated  $B_0$  was correct. Because the CEST saturation module for pulse type S had shorter (0.5 ms) pulses, the oscillations were not present in the frequency offset range of interest in the CEST z-spectra. In Figure 3B, extrapolated qMT curves and the CEST data points are shown for the same phantom as in Figure 3A. Note that the extrapolated qMT curves (e.g., dotted lines in Figure 3B) were meant to model only the MT effects and therefore were not expected to overlap with the CEST data points on the CEST z-spectra (e.g., the dots in Figure 3B). Instead, the differences between the 2 curves represent the CEST effect after subtracting the MT effect. All fits have EPG incorporated into the BM simulations to take into account the magnetization residing in higher order echo pathways that are refocused by successive RF pulses. MT plots with and without EPG are shown in Supporting Information Figure S1, showing improved model fits when EPG is included.

Figure 4 shows plots of 2 estimated MT parameters, the relative semi-solid fraction ( $M_0^B$ ) and the  $T_2$  relaxation time of the semi-solid pool ( $T_2^B$ ), for all phantom experiments with both pulse types at 3T and pulse type S at 1.5T. At 3T, for the tube with 2% agar, there was no significant difference in  $M_0^B$  (by the Wilcoxon rank-sum test) between pulse types L and S. The estimated relative semi-solid fraction was expected to be similar across the different concentrations of  $\text{NH}_4\text{Cl}$  because of the constant concentration of 2% agar in each vial that was responsible for MT effects. However, the estimated  $M_0^B$  value increased with concentration of  $\text{NH}_4\text{Cl}$  (for both pulse types at 3T and at 1.5T compared to 2% agar), suggesting that the MT parameter estimates are affected by CEST contributions. At 1.5T, the  $M_0^B$  value for 2% agar (with  $M_0^B = 0.63\%$  [confidence interval (CI) = 0.49, 0.74]) was significantly higher than that of 3T ( $M_0^B = 0.46\%$  [CI = 0.39, 0.50]) for pulse type S. The fitted semi-solid  $T_2^B$  values ranged from 14.8–16.0  $\mu\text{s}$  for pulse type L at 3T, from 11.2–17.2  $\mu\text{s}$  for pulse type S at 3T, and from 15.3–18.0  $\mu\text{s}$  for pulse type S at 1.5T. The exchange rate,  $R$ , is not shown as it had large confidence intervals (of up to approximately  $\pm 1200$  Hz) and was difficult to determine in this phantom experiment. This is consistent with the high levels of uncertainty previously reported in the exchange rates,<sup>25</sup> in which estimated rates varied significantly depending on different subsets of data used.

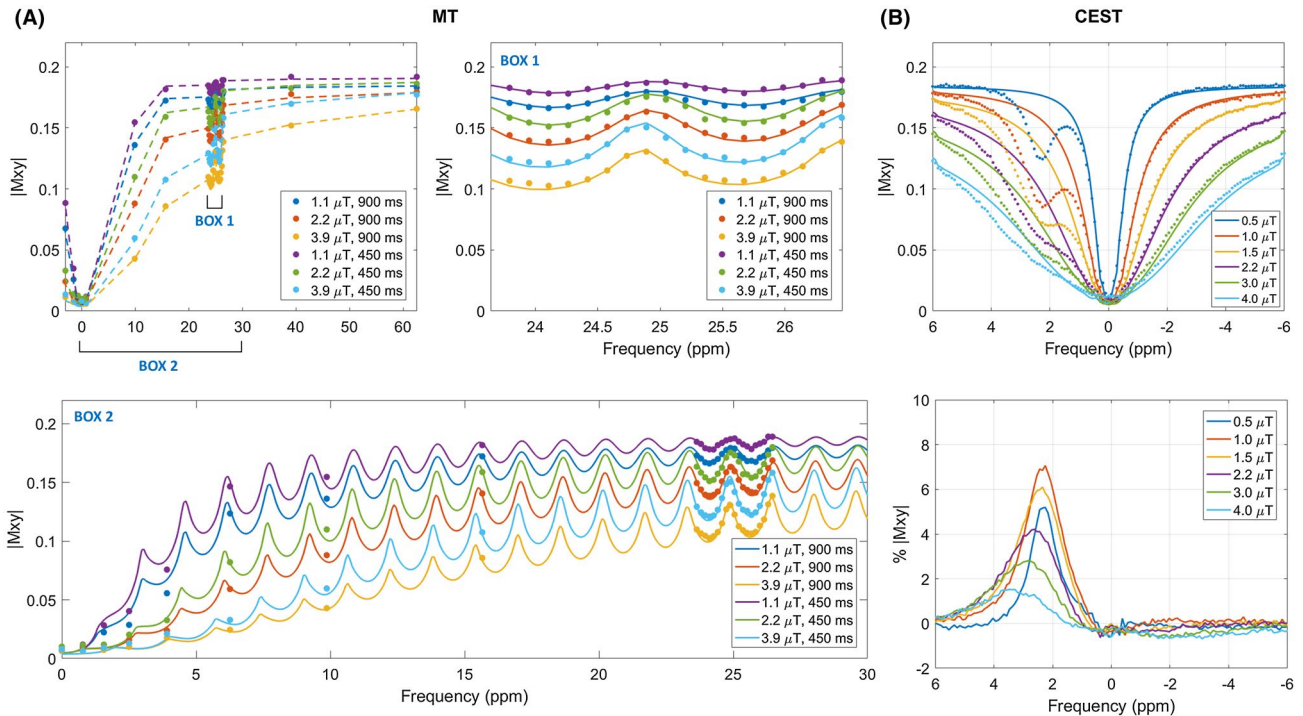


**FIGURE 3** Fitted MT and CEST curves at 1.5T. (A) Phantom data (dots) and model fits (dashed lines) are shown for 2% agar with 1.0M  $\text{NH}_4\text{Cl}$ , acquired using pulse type S. Boxes 1 and 2 show the model fits (solid lines) simulated at closely spaced frequency offsets to illustrate the signal oscillations. The purpose of the dashed lines is to guide the eye and do not represent the model at frequencies in between the acquired data points. In box 1, both the model and data points are shown (1510–1690 Hz). In box 2, the model was evaluated from 0–2000 Hz, every 5Hz. (B) In the same phantom, extrapolated qMT curves (solid lines) and acquired CEST spectra (dots) are shown. In the bottom plot, the differences (between the extrapolated curves and CEST data points, representing the CEST effect) are plotted for each  $B_1$  amplitude after subtracting the MT effects

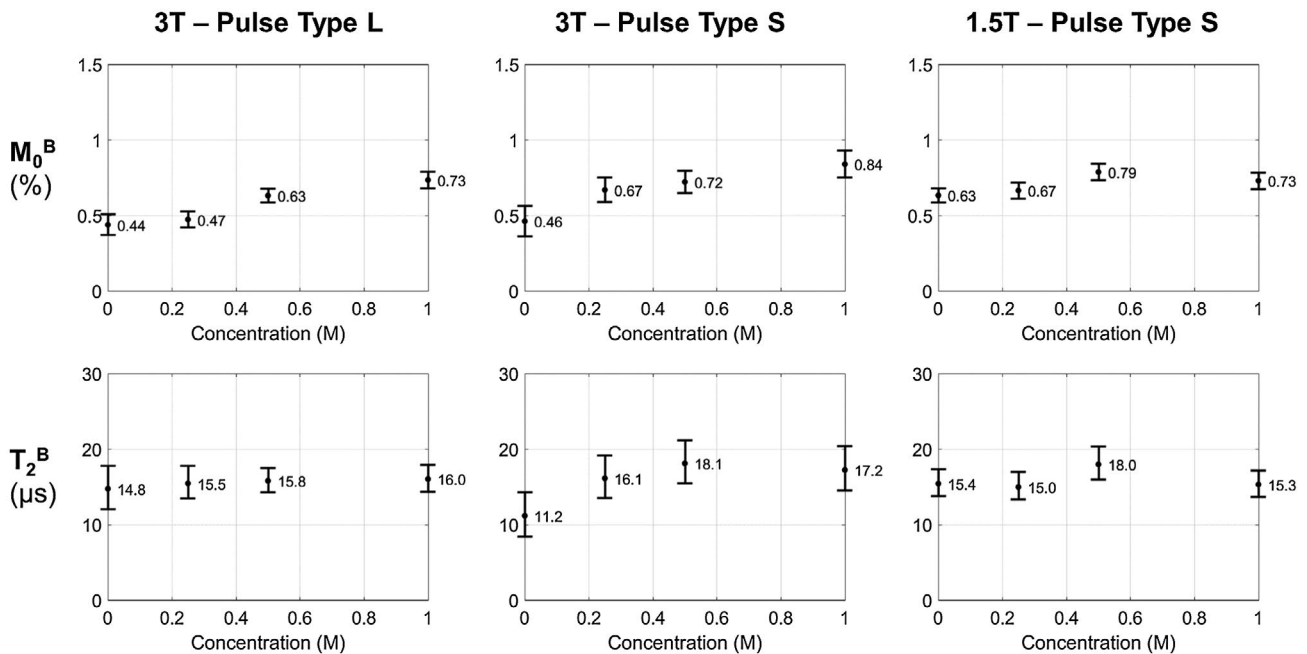


**FIGURE 4** Comparison of long (L) and short (S) pulsed saturation schemes for magnetization transfer: Parameter estimates for the equilibrium magnetization of the semi-solid pool ( $M_0^B$ ) and the  $T_2$  relaxation time of the semi-solid pool ( $T_2^B$ ) are shown for all 3 phantom experiments (using pulse type L at 3T, pulse type S at 3T, and pulse type S at 1.5T), for different concentrations of  $\text{NH}_4\text{Cl}$  with 2% agar (0 M, 0.25 M, 0.5 M, and 1.0 M). Solid black dots represent the pixelwise parameter estimates (mean value over each region-of-interest [ROI]), and the error bars represent the 68% CI. The mean values are displayed for each data point

A comparison of model fits between the 2 saturation schemes, both implemented at 3T, are shown in Supporting Information Figure S2. The differences in the effect of EPG are also shown. The EPG effects were largely dominated by the number of spoilers used. For MT, longer pulses and a substantially reduced number of spoilers were used in pulse type L ( $N_{\text{spoil}} = 4$ ) compared to pulse type S ( $N_{\text{spoil}} \geq 45$ ). As such, model fits from pulse type L were less dependent on the use of EPG (as shown in Supporting Information Figure S2A). In spectra acquired with pulse type S, large discrepancies were seen between the model and data points without EPG (as shown in Supporting Information Figure S2C). In the CEST sequence, where  $N_{\text{spoil}} = 4$  in pulse type L and  $N_{\text{spoil}} = 9$  in pulse type S, improved fits were seen near the central part of the water resonance when EPG was included (as shown in Supporting Information Figures S2B and S2D), with greater misfits in pulse scheme S when EPG was not used.

In Figure 5, the amine CEST effect and CEST asymmetry values are plotted for each concentration of  $\text{NH}_4\text{Cl}$  (0 M, 0.25 M, 0.5 M, and 1.0 M) with 2% agar. The CEST parameters are shown for the 3 phantom experiments. Both the amine CEST effect and asymmetry increase with increasing  $\text{NH}_4\text{Cl}$  concentration. At 3T, the CEST quantities between pulse types L and S can be directly compared at  $B_{1,\text{RMS}} = 1.0 \mu\text{T}$ , which

maximized the CEST effect and asymmetry compared to other sampled  $B_1$  amplitudes. At 1.5T, the CEST parameters were maximized at  $B_{1,\text{RMS}} = 0.5 \mu\text{T}$ . At these  $B_{1,\text{RMS}}$  values, chosen to maximize the CEST effect, it can be seen that the CEST effect and asymmetry values are comparable between the pulse types and across field strengths. For the vial with the highest concentration of  $\text{NH}_4\text{Cl}$ , the amine CEST effect had values between 0.06–0.08, whereas the CEST asymmetry had values between 0.3–0.4. The CEST asymmetry is expected to be 0 in the vial with pure agar. The small non-negative value of the CEST effect at 0 M of  $\text{NH}_4\text{Cl}$  is attributable to small errors in the qMT-extrapolated curve.

For the 3-pool CEST parameter fits at 3T, there was agreement in the relative CEST pool fraction,  $M_0^{\text{C}}$ , between pulse types L and S, with  $M_0^{\text{C}} = 3.7\%$  (CI = 3.5,3.9) using pulse type L and  $M_0^{\text{C}} = 3.8\%$  (CI = 3.5,4.1) using pulse type S. The value of  $M_0^{\text{C}}$  was higher at 1.5T, with  $M_0^{\text{C}} = 4.1$  (CI = 4.0,4.2), compared to values at 3T. The exchange rate between the water and CEST pools ( $R^{\text{C}}$ ) was similar at 3T, with  $R^{\text{C}} = 53\text{Hz}$  (CI = 49,58) using pulse type L and  $R^{\text{C}} = 50\text{Hz}$  (CI = 46,55) using pulse type S. However, it was lower at 1.5T with  $R^{\text{C}} = 34\text{Hz}$  (CI = 33,36). The full comparison is presented in Table 1.

Figure 6 displays example maps of the healthy brain at 1.5T and 3T. Differentiation of white and gray matter was

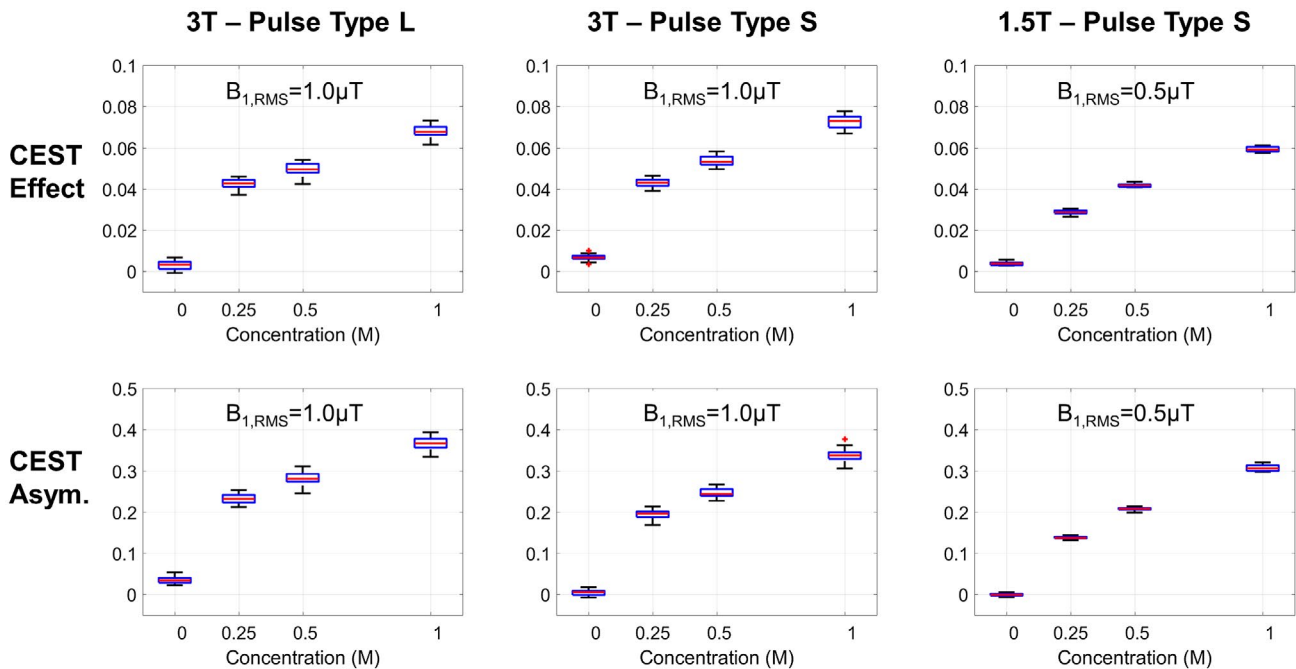


**FIGURE 5** Comparison of long (L) and short (S) pulsed saturation schemes for CEST in phantom: The amide CEST effect and CEST asymmetry values are plotted for each concentration of  $\text{NH}_4\text{Cl}$  (0 M, 0.25 M, 0.5 M, and 1.0 M) with 2% agar. The CEST parameters have been averaged between 2–3 ppm, and are shown for 3 phantom experiments (i.e., pulse type L at 3T, pulse type S at 3T, and pulse type S at 1.5T). The CEST effect and asymmetry were compared at the  $B_1$  amplitudes that generated the maximum value, with  $B_1 = 1.0 \mu\text{T}$  for pulse type L at 3T,  $B_{1,\text{RMS}} \approx \frac{1}{2} \times B_{1,\text{max}} = 1.0 \mu\text{T}$  for pulse type S at 3T, and  $B_{1,\text{RMS}} = 0.5 \mu\text{T}$  for pulse type S at 1.5T. On each box, the central mark (red line) indicates the median value over the pixels in each ROI. The bottom and top edges of the box indicate the 25th and 75th percentiles, respectively. The whiskers extend to the most extreme data points (not including the outliers) and the outliers are denoted by +

**TABLE 1** Quantitative CEST parameter estimates in phantom experiment

	Pulse type L 3T	Pulse type S 3T	Pulse type S 1.5T
$M_0^C$ (%)	3.7 (3.5, 3.9)	3.8 (3.5, 4.1)	4.1 (4.0, 4.2)
$T_2^C$ (ms)	12.8 (12.0, 13.0)	11.0 (10.3, 11.9)	13.3 (13.0, 13.6)
$R^C$ (Hz)	53.4 (48.7, 58.2)	50.4 (45.7, 55.2)	34.4 (33.0, 35.7)

Estimated values of the equilibrium magnetization of the CEST pool ( $M_0^C$ ), the  $T_2$  of the CEST pool ( $T_2^C$ ), and the exchange rate between the water and CEST pools ( $R^C$ ) for 1.0 M  $\text{NH}_4\text{Cl}$  with 2% agar. The 68% CIs are displayed in brackets.

seen in the brain at both field strengths, with improved white-gray matter contrast at 3T. Corresponding MT and CEST z-spectra for a region in the white matter are shown in Figure 7. For the MT curves, good overlap can be seen between the MT model and the data points. Over a white matter region, the mean semi-solid percentages were  $18 \pm 2\%$  for 3T and  $15 \pm 2\%$  for 1.5T. Whereas the amide CEST maps had comparable intensities between 3T and 1.5T (Figure 6), with mean white matter contributions of  $(1.0 \pm 0.3) \times 10^{-2}$  and  $(0.7 \pm 0.2) \times 10^{-2}$ , respectively, there were notable differences in the CEST asymmetry and NOE. There was a larger NOE contribution of  $(2.6 \pm 0.3) \times 10^{-2}$  at 3T compared to  $(0.7 \pm 0.2) \times 10^{-2}$  at 1.5T. This is visible in the maps (Figure 6), as well as in the corresponding CEST z-spectra (Figure 7). The CEST asymmetry values in white matter were negative ( $-4.9 \pm 0.4\%$ ) at 3T and  $(0.0 \pm 0.3\%)$  at 1.5T using the sets of  $B_1$  amplitudes that were tested. A summary of the key findings of this study is provided in Supporting Information Table S4.

## 4 | DISCUSSION

To date, only a limited number of in vivo CEST studies have been performed at 1.5T.<sup>41,42</sup> Although only short pulse durations could be implemented on the 1.5T scanner because of RF amplifier limitations, the repetitive pulse scheme (with gaps between pulses) used in the present study is a viable alternative method that provides enough saturation to detect the CEST effect. For both the MT and CEST quantification, it is important that the correct pulse sequence parameters be included in the Bloch simulation model. As well, using the EPG framework to model the repetitive saturation pulses improves the accuracy of the fits, as demonstrated in phantom experiments. The effects are more substantial when numerous spoiler gradients are present, such as in the saturation module used in the MT experiments. EPG methods, including EPG-X,<sup>32</sup> tend to consider RF pulses as instant. Our approach does not assume instantaneous RF pulses and therefore could be used more generally to account for relaxation effects during long RF pulses. However, a drawback is that our approach requires more intensive computation because of numerous matrix multiplications.

Block RF pulses are simpler to model compared to shaped pulses because each segment has a piecewise constant amplitude. For shaped pulses (e.g., Gaussian or sinc pulses), the

time-varying amplitudes need to be approximated as a series of piecewise constant pulses (e.g., 50  $\mu\text{s}$  in duration)<sup>25</sup> in the BM simulations<sup>25,31</sup> to allow for the propagation of magnetization through each interval. Other approximations that have been proposed<sup>24,43,44</sup> are discussed by Portnoy and Stanis.<sup>25</sup>

Results from phantom experiments, performed to compare 2 different types of saturation pulses, showed that the model is well fitted to the data points for both long (L) and short (S) pulsed schemes. The aim of the present work was to isolate CEST effects from other contributions including  $T_1$ ,  $T_2$ , MT,  $B_0$ , and  $B_1$ . In addition to estimating quantitative CEST parameters using a 3-pool BM model in phantom experiments, the approach of Heo et al.<sup>40</sup> was also used, where the CEST data points were subtracted from extrapolated qMT curves. This approach is useful for the relatively low APT effects at 1.5T, where it may not be applicable to directly fit the data using additional CEST pools in the BM model.

Discrepancies in parameter values between continuous and pulsed saturation methods have been reported in Portnoy and Stanis.<sup>25</sup> Although the pulsed saturation schemes (L and S) resulted in a non-steady-state signal, this has been taken into account by fitting with BM simulations that include the exact pulse sequence parameters (instead of fitting to the analytic steady-state solution). Some differences in fitted MT parameters between the (L and S) pulsed schemes could mean that the data is incompletely described by the 2- and 3-pool BM models. Differences in the estimated semi-solid fraction between 1.5T and 3T experiments could have been related to systematic or scanner-dependent errors. In the presence of CEST, results showed that the different pulse types may have led to inaccuracies of the semi-solid fraction estimates. However, in the absence of CEST (in 2% agar), and when performed on the same scanner (3T), the 2 pulse types produced similar estimates of the semi-solid fraction. Hypothesized reasons for the large variability in estimated exchange rates include the presence of systematic errors related to off-resonance or RF amplitudes, and possibly, the insensitivity of the experimental data to the exchange rate parameter.<sup>25</sup>

In the in vivo scans at 3T, the mean MT semi-solid fraction ( $M_0^B = 18 \pm 2\%$ ) found in our study is higher than that reported in healthy controls by Mehrabian et al.<sup>45</sup> ( $14.7 \pm 1.0\%$ ), also at 3T. This could be the result of different fitting methods used.<sup>45</sup> Non-zero CEST amide and NOE areas were detected in vivo at 1.5T using the MT-extrapolation method.<sup>40</sup>

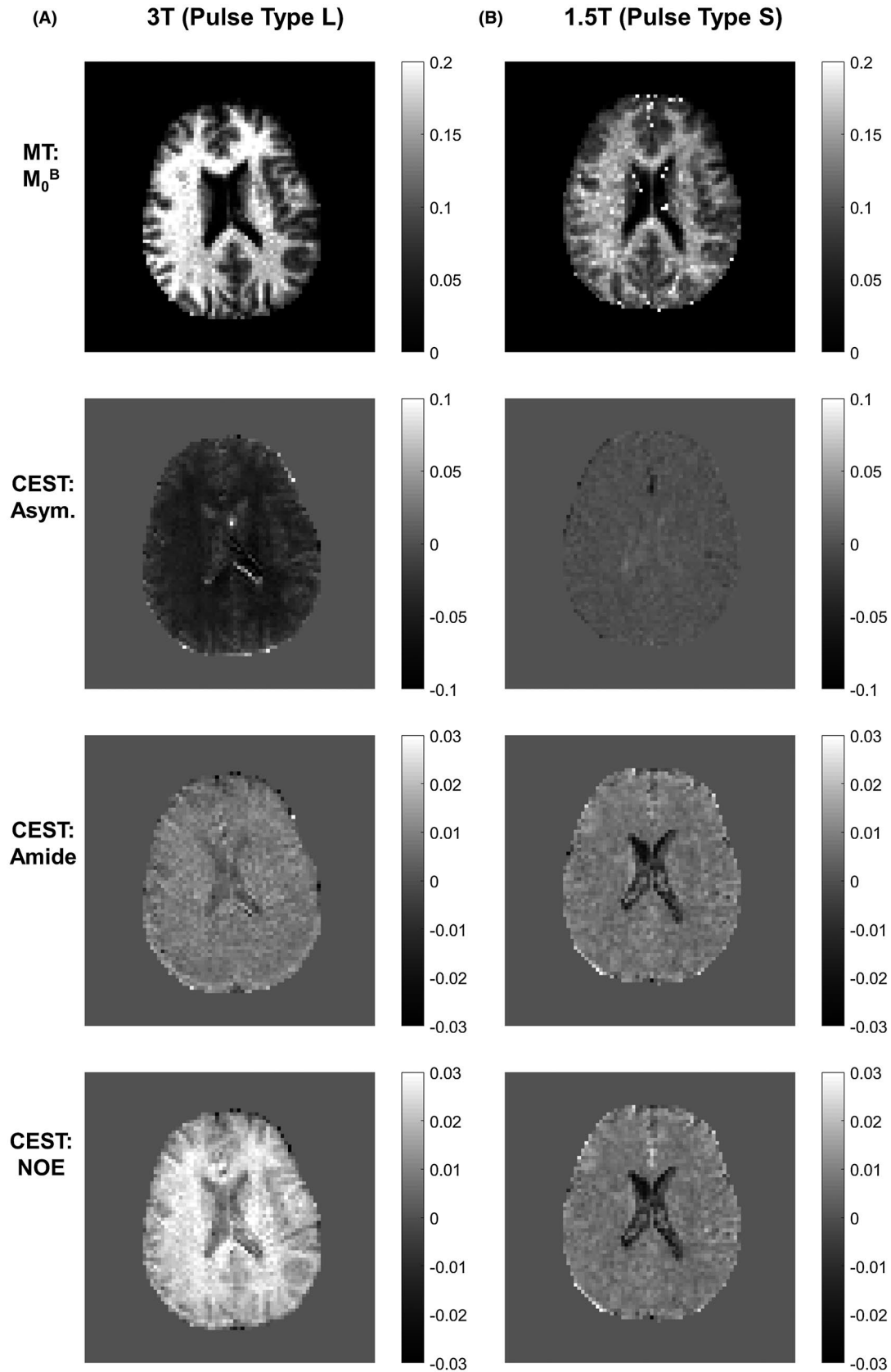


**FIGURE 6** Saturation transfer maps at 3T and 1.5T in the healthy brain. Maps are shown of a similar slice in the brain of the same healthy subject, scanned at (A) 3T (with saturation pulse type L) and (B) at 1.5T (with saturation pulse type S). The CEST maps have been interpolated to  $B_{1,RMS} = 0.6 \mu\text{T}$  for 3T, and  $B_{1,RMS} = 1.5 \mu\text{T}$  for 1.5T

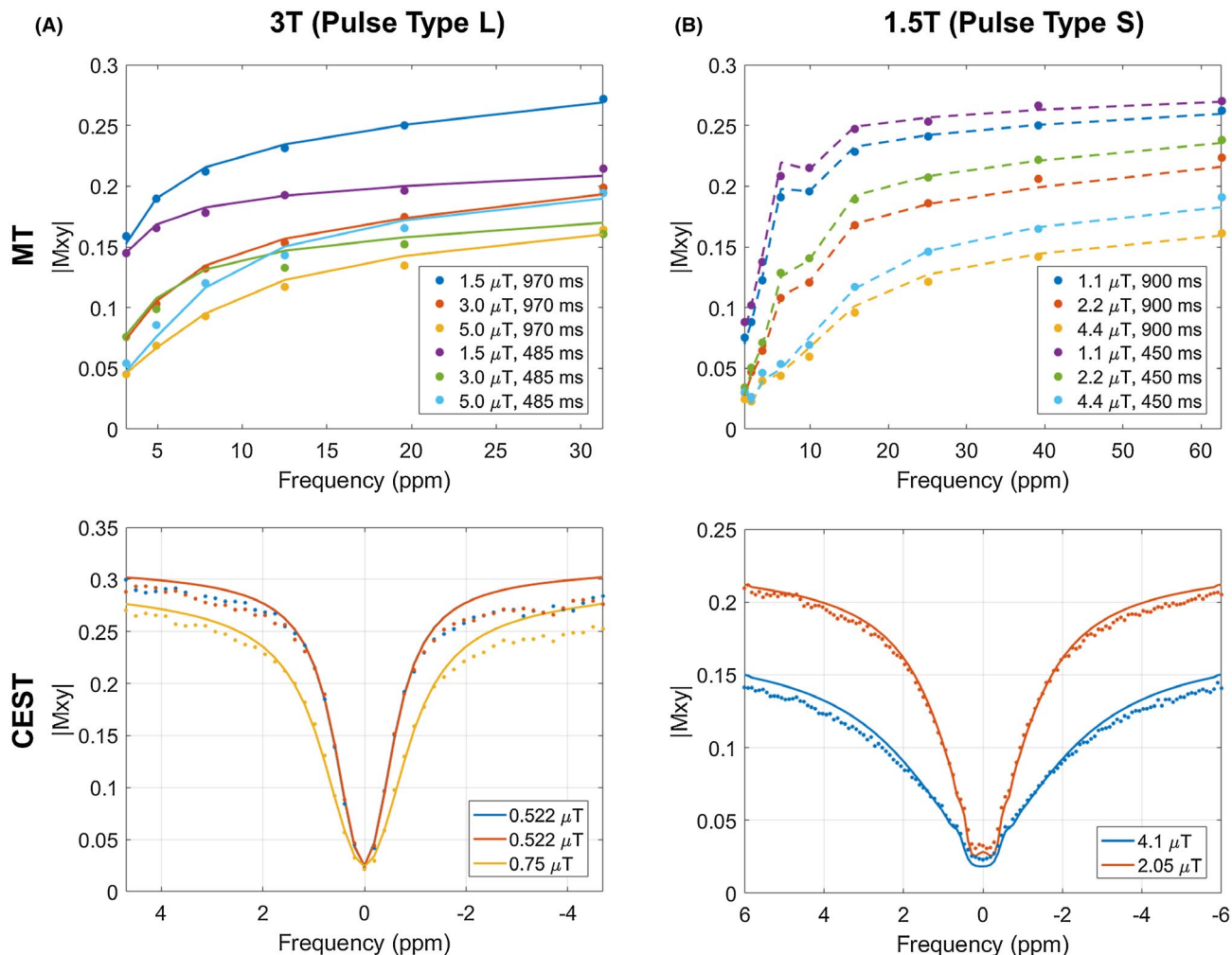


**FIGURE 7** Saturation transfer model fits at 3T and 1.5T in the healthy brain. Fitted MT curves with MT data (top) and MT-extrapolated curves with CEST data (bottom) are shown for an ROI in the white matter of a healthy brain. Model fits are shown by the solid lines and the data are represented by the dots. Z-spectra from the 2 pulsed saturation schemes are shown: (A) with long (L) pulses implemented on the 3T system, and (B) a short (S) pulses implemented on the 1.5T system. The legend shows the maximum  $B_1$  amplitudes for pulse type S and RMS  $B_1$  amplitudes for pulse type L. At 3T, a nuclear Overhauser enhancement (NOE) peak is visible at around  $-3$  ppm

The CEST asymmetry value in the healthy brain at 3T ( $\text{CEST}_{\text{asym}} = -4.9 \pm 0.4\%$ ) obtained in our study are more negative than those of Mehrabian et al. ( $\text{CEST}_{\text{asym}} = -3.9 \pm 0.3\%$ ). Across different field strengths, the CEST contributions, and therefore, asymmetry, are dependent on parameters such as  $B_1$  and frequency offset. Compared to 3T, the smaller NOE effect at 1.5T contributed to a more positive CEST asymmetry at 1.5T. Our results showed that, qualitatively, the asymmetry maps at 1.5T were not as useful for distinguishing between white and gray matter compared to those at 3T. The near-zero asymmetry detected at 1.5T was related to differences in the field strength or the choice of  $B_1$  and not the result of using long or short pulses. Detection of the amide and NOE CEST areas was based on the assumption that any errors in the MT-extrapolated curves were smaller than the true CEST contribution (because the areas were based on the difference between the CEST data points and the MT-extrapolated values). If there

were systematic errors in the MT-extrapolation, for example, that caused the MT-extrapolated curve to have lower values, then the amide/NOE CEST effect would appear to be larger than its true contribution. The CEST asymmetry, on the other hand, was relatively insensitive to extrapolation errors because these errors would have cancelled out because of the symmetry of the extrapolated MT curves about the water peak.

This study has several limitations. It has been shown that the spoiled gradient echo signal, as in the VFA sequence, changes with MT as well as the flip angle and TR.<sup>46</sup> Although flip angle and TR were accounted for in the estimation of  $T_1^{\text{OBS}}$  using the VFA method, MT effects were not considered.  $T_2^*$  effects were not accounted for by the  $T_2$  fitting procedure through which the observed  $T_2$  was estimated. The current EPG approach does not model any  $T_2^*$  effects. However, the observed  $T_2$  was only used as an initial guess for the estimation of the  $T_2$  of the water pool ( $T_2^A$ ), which was subsequently refined

by fitting the water peak. For the in vivo experiment at 3T, only pulse type L was used, and the scan was not repeated for both pulse types at 3T. Fitting the Bloch simulation model using a pulsed qMT sequence has lengthy processing times compared to a steady-state approach where analytic formulas are applicable. In the future, analytic approaches to approximate the signal could be explored instead.<sup>47</sup> In this study, measures were taken to account for the effects of  $B_0$  (to which CEST parameters including asymmetry are especially sensitive) and also to remove other effects including  $T_1$  and  $T_2$ . However, there could be residual effects in the estimated CEST parameters that are not purely from CEST. Because of the small magnitude of the CEST effect in vivo, the robustness of CEST at 1.5T will need to be determined by performing studies in patients with brain tumors.

## 5 | CONCLUSIONS

A pulsed saturation scheme was used to overcome the single RF amplifier duty cycle limitations of the 1.5T clinical scanner. MT and CEST parameters were quantified in phantoms and in the healthy brain at both 1.5T and 3T. Parameters were estimated using a BM simulation that incorporated the extended phase graph formalism. The new methods demonstrated promise for enabling broader application of CEST MRI for field strengths below 3T.

## ACKNOWLEDGMENTS

The authors acknowledge sources of funding from NSERC (RGPIN-2017-06596, CRD 507521-16), Terry Fox (New Frontiers Program Project Grant) and CIHR. The authors thank Wilfred Lam for useful suggestions.

## ORCID

Rachel W. Chan  <https://orcid.org/0000-0003-0475-1111>

## REFERENCES

- Wolff SD, Balaban RS. Magnetization transfer contrast (MTC) and tissue water proton relaxation in vivo. *Magn Reson Med*. 1989;10:135–144.
- Henkelman RM, Huang X, Xiang QS, Stanisz GJ, Swanson SD, Bronskill MJ. Quantitative interpretation of magnetization transfer. *Magn Reson Med*. 1993;29:759–766.
- Wolff SD, Balaban RS. NMR imaging of labile proton exchange. *J Magn Reson*. 1990;86:164–169.
- Ward KM, Aletras AH, Balaban RS. A new class of contrast agents for MRI based on proton chemical exchange dependent saturation transfer (CEST). *J Magn Reson*. 2000;143:79–87.
- van Zijl PCM, Lam WW, Xu J, Knutsson L, Stanisz GJ, Knutsson L, Stanisz GJ. Magnetization transfer contrast and chemical exchange saturation transfer MRI. Features and analysis of the field-dependent saturation spectrum. *NeuroImage*. 2018;168:222–241.
- Jones KM, Pollard AC, Pagel MD. Clinical applications of chemical exchange saturation transfer (CEST) MRI. *J Magn Reson Imaging*. 2018;47:11–27.
- Jones CK, Schlosser MJ, van Zijl PC, Pomper MG, Golay X, Zhou J. Amide proton transfer imaging of human brain tumors at 3T. *Magn Reson Med*. 2006;56:585–592.
- Zhou J, Zhu HE, Lim M, et al. Three-dimensional amide proton transfer MR imaging of gliomas: initial experience and comparison with gadolinium enhancement. *J Magn Reson Imaging*. 2013;38:1119–1128.
- Scheidegger R, Wong ET, Alsop DC. Contributors to contrast between glioma and brain tissue in chemical exchange saturation transfer sensitive imaging at 3 Tesla. *NeuroImage*. 2014;99:256–268.
- Ma BO, Blakeley JO, Hong X, et al. Applying amide proton transfer-weighted MRI to distinguish pseudoprogression from true progression in malignant gliomas. *J Magn Reson Imaging*. 2016;44:456–462.
- Mehrabian H, Myrehaug S, Soliman H, Sahgal A, Stanisz GJ. Evaluation of glioblastoma response to therapy with chemical exchange saturation transfer. *Int J Radiat Oncol Biol Phys*. 2018;101:713–723.
- Mehrabian H, Desmond KL, Soliman H, Sahgal A, Stanisz GJ. Differentiation between radiation necrosis and tumor progression using chemical exchange saturation transfer. *Clin Cancer Res*. 2017;23:3667–3675.
- Jiang S, Eberhart CG, Lim M, et al. Identifying recurrent malignant glioma after treatment using amide proton transfer-weighted MR imaging: a validation study with image-guided stereotactic biopsy. *Clin Cancer Res*. 2019;25:552–561.
- Park JE, Kim HS, Park KJ, Kim SJ, Kim JH, Smith SA. Pre- and posttreatment glioma: comparison of amide proton transfer imaging with MR spectroscopy for biomarkers of tumor proliferation. *Radiology*. 2015;278:514–523.
- Togao O, Yoshiura T, Keupp J, et al. Amide proton transfer imaging of adult diffuse gliomas: correlation with histopathological grades. *Neuro Oncol*. 2014;16:441–448.
- Regnery S, Adeberg S, Dreher C, et al. Chemical exchange saturation transfer MRI serves as predictor of early progression in glioblastoma patients. *Oncotarget*. 2018;9:28772–28783.
- Mehrabian H, Myrehaug S, Soliman H, Sahgal A, Stanisz GJ. Quantitative magnetization transfer in monitoring glioblastoma (GBM) response to therapy. *Sci Rep*. 2018;8:2475.
- Zaiss M, Windschuh J, Paech D, et al. Relaxation-compensated CEST-MRI of the human brain at 7 T: unbiased insight into NOE and amide signal changes in human glioblastoma. *NeuroImage*. 2015;112:180–188.
- Zaiss M, Windschuh J, Goerke S, et al. Downfield-NOE-suppressed amide-CEST-MRI at 7 Tesla provides a unique contrast in human glioblastoma. *Magn Reson Med*. 2017;77:196–208.
- Paech D, Zaiss M, Meissner J-E, et al. Nuclear overhauser enhancement mediated chemical exchange saturation transfer imaging at 7 Tesla in glioblastoma patients. *PLoS ONE*. 2014;9:e104181.
- Paech D, Windschuh J, Oberhollenzer J, et al. Assessing the predictability of IDH mutation and MGMT methylation status in glioma patients using relaxation-compensated multi-pool CEST MRI at 7.0 Tesla. *Neuro Oncol*. 2018;20:1661–1671.

22. Desmond KL, Mehrabian H, Chavez S, et al. Chemical exchange saturation transfer for predicting response to stereotactic radiosurgery in human brain metastasis. *Magn Reson Med.* 2017;78:1110–1120.
23. Graham SJ, Henkelman RM. Understanding pulsed magnetization transfer. *J Magn Reson Imaging.* 1997;7:903–912.
24. Sled JG, Pike GB. Quantitative imaging of magnetization transfer exchange and relaxation properties in vivo using MRI. *Magn Reson Med.* 2001;46:923–931.
25. Portnoy S, Stanisz GJ. Modeling pulsed magnetization transfer. *Magn Reson Med.* 2007;58:144–155.
26. Sun PZ, Benner T, Kumar A, Sorensen AG. Investigation of optimizing and translating pH-sensitive pulsed-chemical exchange saturation transfer (CEST) imaging to a 3T clinical scanner. *Magn Reson Med.* 2008;60:834–841.
27. Zu Z, Li K, Janve VA, Does MD, Gochberg DF. Optimizing pulsed-chemical exchange saturation transfer imaging sequences. *Magn Reson Med.* 2011;66:1100–1108.
28. Meissner JE, Goerke S, Rerich E, et al. Quantitative pulsed CEST-MRI using  $\Omega$ -plots. *NMR Biomed.* 2015;28:1196–1208.
29. Tyler DJ, Gowland PA. Rapid quantitation of magnetization transfer using pulsed off-resonance irradiation and echo planar imaging. *Magn Reson Med.* 2005;53:103–109.
30. Desmond KL, Stanisz GJ. Understanding quantitative pulsed CEST in the presence of MT. *Magn Reson Med.* 2012;67:979–990.
31. Harris RJ, Cloughesy TF, Liau LM, et al. Simulation, phantom validation, and clinical evaluation of fast pH-weighted molecular imaging using amine chemical exchange saturation transfer echo planar imaging (CEST-EPI) in glioma at 3 T. *NMR Biomed.* 2016;29:1563–1576.
32. Malik SJ, Teixeira R, Hajnal JV. Extended phase graph formalism for systems with magnetization transfer and exchange. *Magn Reson Med.* 2018;80:767–779.
33. Weigel M. Extended phase graphs: dephasing, RF pulses, and echoes - pure and simple. *J Magn Reson Imaging.* 2015;41:266–295.
34. Hennig J. Echoes - how to generate, recognize, use or avoid them in MR-imaging sequences. Part I: fundamental and not so fundamental properties of spin echoes. *Concepts Magn Reson Part A.* 1991;3:125–143.
35. Schuenke P, Windschuh J, Roeloffs V, Ladd ME, Bachert P, Zaiss M. Simultaneous mapping of water shift and B1(WASABI)-application to field-inhomogeneity correction of CEST MRI data. *Magn Reson Med.* 2017;77:571–580.
36. Kim M, Gillen J, Landman BA, Zhou J, van Zijl PC. Water saturation shift referencing (WASSR) for chemical exchange saturation transfer (CEST) experiments. *Magn Reson Med.* 2009;61:1441–1450.
37. Cheng HL, Wright GA. Rapid high-resolution T(1) mapping by variable flip angles: accurate and precise measurements in the presence of radiofrequency field inhomogeneity. *Magn Reson Med.* 2006;55:566–574.
38. Pike GB. Pulsed magnetization transfer contrast in gradient echo imaging: a two-pool analytic description of signal response. *Magn Reson Med.* 1996;36:95–103.
39. Morrison C, Mark HR. A model for magnetization transfer in tissues. *Magn Reson Med.* 1995;33:475–482.
40. Heo HY, Zhang Y, Jiang S, Lee DH, Zhou J. Quantitative assessment of amide proton transfer (APT) and nuclear overhauser enhancement (NOE) imaging with extrapolated semisolid magnetization transfer reference (EMR) signals: II. Comparison of three EMR models and application to human brain glioma at 3 Tesla. *Magn Reson Med.* 2016;75:1630–1639.
41. Dixon WT, Ren J, Lubag AJM, et al. A concentration-independent method to measure exchange rates in PARACEST agents. *Magn Reson Med.* 2010;63:625–632.
42. Dagher AP, Aletras A, Choyke P, Balaban RS. Imaging of urea using chemical exchange-dependent saturation transfer at 1.5 T. *J Magn Reson Imaging.* 2000;12:745–748.
43. Ramani A, Dalton C, Miller DH, Tofts PS, Barker GJ. Precise estimate of fundamental in-vivo MT parameters in human brain in clinically feasible times. *Magn Reson Imaging.* 2002;20:721–731.
44. Yarnykh VL. Pulsed Z-spectroscopic imaging of cross-relaxation parameters in tissues for human MRI: theory and clinical applications. *Magn Reson Med.* 2002;47:929–939.
45. Mehrabian H, Lam WW, Myrehaug S, Sahgal A, Stanisz GJ. Glioblastoma (GBM) effects on quantitative MRI of contralateral normal appearing white matter. *J Neurooncol.* 2018;139:97–106.
46. Ou X, Gochberg DF. MT effects and T<sub>1</sub> quantification in single-slice spoiled gradient echo imaging. *Magn Reson Med.* 2008;59:835–845.
47. Xiao G, Sun PZ, Wu R. Fast simulation and optimization of pulse-train chemical exchange saturation transfer (CEST) imaging. *Phys Med Biol.* 2015;60:4719–4730.

## SUPPORTING INFORMATION

Additional supporting information may be found online in the Supporting Information section at the end of the article.

**FIGURE S1** Effect of EPG on qMT spectra. Phantom data points (dots) and fitted model (lines) are shown for 2% agar with 1.0 M NH<sub>4</sub>Cl, imaged at 1.5T. The purpose of the dashed lines is to guide the eye and do not represent the model at frequencies in between the acquired data points. Quantitative MT fits are shown (A) without EPG and (B) with EPG incorporated into the Bloch-McConnell model. Zoomed-in plots of the model and data are shown in the bottom row for the finely sampled frequency offset range (1510–1690 Hz, at 10-Hz intervals) and illustrates oscillation in the signal

**FIGURE S2** Comparison of fitted curves for long (L) and short (S) pulsed saturation schemes in 2% agar. The data points (dots) and fitted model (dashed lines for MT and solid lines for CEST) are shown for the saturation schemes (A and B) with long (L) pulses and (C and D) with short (S) pulses, imaged on a 3T system where both long and short pulse types could be implemented. The 1st column shows model fits without EPG and the 2nd column shows fits with EPG included. Discrepancies between the fitted model and data without EPG are indicated by the arrows

**TABLE S1** Saturation pulse sequence parameters for phantom experiments. Parameters for the MT and CEST sequences are shown for phantom experiments performed at 1.5T (with pulse type S) and 3T (with pulse types S and L). The reference frequency offset is represented by “ref,” followed by the

multiplicative factor N. For example, “ref×N” indicates that the frequency offset of 100,000 Hz is repeated N times before subsequent saturation frequency offsets. The colon separates the start, step and end frequency offsets. Pulses in the MT sequence were separated by 2.5-ms gaps with spoiling gradients in between each pulse. For the CEST sequence, the sets of 125 rectangular pulses (with duration of 0.5 ms each and gaps of 0.5 ms) were shaped to a Fermi amplitude modulation function, with 9 repetitions of the Fermi-modulated pulses

**TABLE S2** Saturation protocol for in vivo imaging at 1.5T and 3T. Parameters for the MT and CEST brain imaging scans are shown. For the MT sequence at 3T, the shot intervals were variable and were increased for the highest B<sub>1</sub> because of SAR limitations

**TABLE S3** Pulse sequence parameters for B<sub>1</sub>/B<sub>0</sub>/T<sub>1</sub>/T<sub>2</sub> mapping. Parameters are shown for the water shift and B<sub>1</sub> (WASABI) sequence (used for B<sub>0</sub> and B<sub>1</sub> mapping), T<sub>1</sub>-weighted FFE sequence (for T<sub>1</sub> mapping), and T<sub>2</sub>-weighted sequence (for T<sub>2</sub> mapping) for 1.5T and 3T phantom experiments

**TABLE S4** Summary of key results. The main results from phantom and in vivo experiments are summarized for comparisons across different pulse types (L and S) and across field strengths (1.5T and 3T). All results in this table were obtained after including extended phase graphs in the modeling

**How to cite this article:** Chan RW, Myrehaug S, Stanisz GJ, Sahgal A, Lau AZ. Quantification of pulsed saturation transfer at 1.5T and 3T. *Magn Reson Med.* 2019;82:1684–1699. <https://doi.org/10.1002/mrm.27856>

**APPENDIX**

The theoretical description of extended phase graphs (EPG) can be found in literature.<sup>32-34</sup> The EPG framework keeps track of magnetization for various pulse sequences. The BM simulations were performed in the EPG basis by transforming M(r) = (M<sub>x</sub>, M<sub>y</sub>, M<sub>z</sub>) to the EPG {F<sub>n</sub>, Z<sub>n</sub>} basis. The Bloch equations describing the magnetization in a 2-pool (water and semi-solid) model in the presence of exchange and RF irradiation are

$$\frac{d}{dt} \begin{pmatrix} M_x^A \\ M_y^A \\ M_z^A \\ M_z^B \end{pmatrix} = \mathbf{A} \begin{pmatrix} M_x^A \\ M_y^A \\ M_z^A \\ M_z^B \end{pmatrix} + \mathbf{C}, \tag{A1}$$

where the water pool is represented by superscript “A” and the semi-solid component pool is represented by superscript “B,” with

$$\mathbf{A} = \begin{pmatrix} -\frac{1}{T_2^A} & -2\pi\Delta & 0 & 0 \\ 2\pi\Delta & -\frac{1}{T_2^A} & -\omega_1 & 0 \\ 0 & \omega_1 & -\frac{1}{T_1^A} - k_{AB} & k_{BA} \\ 0 & 0 & k_{AB} & -\frac{1}{T_1^B} - k_{BA} - W \end{pmatrix} \text{ and } \mathbf{C} = \begin{pmatrix} 0 \\ 0 \\ \frac{M_0^A}{T_1^A} \\ \frac{M_0^B}{T_1^B} \end{pmatrix}$$

and where Δ is the off-resonance frequency of the RF irradiation pulse, ω<sub>1</sub> (= γB<sub>1</sub>) is the angular precession frequency of the off-resonant saturation pulse. Note that the equations assume that the phase of the RF pulse is 0. M<sub>0</sub><sup>A</sup> and M<sub>0</sub><sup>B</sup> are the equilibrium magnetization for the water and semi-solid pools, k<sub>AB</sub>(= RM<sub>0</sub><sup>B</sup>) and k<sub>bA</sub> = (RM<sub>0</sub><sup>A</sup>) are the exchange rates from the water to the semi-solid pool and vice versa, with R being the fundamental exchange constant.<sup>2</sup> The RF absorption rate, W, is defined as W = π × ω<sub>1</sub><sup>2</sup> × g(Δ, T<sub>2</sub><sup>B</sup>), where g(Δ, T<sub>2</sub><sup>B</sup>) is the absorption lineshape of the semi-solid pool. T<sub>1</sub><sup>A</sup> and T<sub>1</sub><sup>B</sup> are the longitudinal recovery time constants, and T<sub>2</sub><sup>A</sup> and T<sub>2</sub><sup>B</sup> are the transverse decay time constants.

Equivalently, this can be written as

$$\frac{d}{dt} \begin{pmatrix} M_+^A \\ M_-^A \\ M_z^A \\ M_z^B \end{pmatrix} = (\mathbf{SAS}^{-1}) \begin{pmatrix} M_+^A \\ M_-^A \\ M_z^A \\ M_z^B \end{pmatrix} + \mathbf{C}, \tag{A2}$$

where

$$M_+ = M_x + iM_y \\ M_- = M_x - iM_y.$$

Analogous to Equations 9A and 9B in Weigel et al.,<sup>32</sup> the corresponding transformation matrices are

$$\mathbf{S} = \begin{pmatrix} 1 & +i & 0 & 0 \\ 1 & -i & 0 & 0 \\ 0 & 0 & 1 & 0 \\ 0 & 0 & 0 & 1 \end{pmatrix}, \tag{A3}$$

$$\mathbf{S}^{-1} = \frac{1}{2} \begin{pmatrix} 1 & 1 & 0 & 0 \\ +i & -i & 0 & 0 \\ 0 & 0 & 2 & 0 \\ 0 & 0 & 0 & 2 \end{pmatrix}. \tag{A4}$$

After Fourier transformation, Equation A2 becomes

$$\frac{d}{dt} \begin{pmatrix} F_+(k) \\ F_-(k) \\ Z^A(k) \\ Z^B(k) \end{pmatrix} = (\mathbf{SAS}^{-1}) \begin{pmatrix} F_+(k) \\ F_-(k) \\ Z^A(k) \\ Z^B(k) \end{pmatrix} + \delta(k) \cdot \mathbf{C}, \tag{A5}$$

where the index  $k$  represents the EPG configuration state.

When the RF amplitude is constant, the solution to the differential Equation A1 is

$$\mathbf{M}(t + \Delta t) = e^{A\Delta t} \mathbf{M}(t) + \mathbf{A}^{-1} (e^{A\Delta t} - \mathbf{I}) \mathbf{C}. \quad (\text{A6})$$

The corresponding solution to the differential Equation A5 (for constant RF amplitude) is

$$\mathbf{F}(t + \Delta t, k) = e^{SAS^{-1}\Delta t} \mathbf{F}(t, k) + \delta(k) \cdot \mathbf{SAS}^{-1} (e^{SAS^{-1}\Delta t} - \mathbf{I}) \mathbf{C}, \quad (\text{A7})$$

where

$$\mathbf{F}(t, k) = [F_+(t, k), F_-(t, k), Z^A(t, k), Z^B(t, k)]^T.$$

Equation A7 was used repeatedly to compute the signal for successive time intervals with duration  $\Delta t$ , each with a constant RF amplitude. The signal from the previous time segment was used as the starting signal for the next segment. The computations were interleaved with the “shift” operator (i.e., Equation 22 in Weigel et al.),<sup>32</sup> which was applied only to segments with spoiling gradients. Note that the second term in Equation A7 was only needed for the zeroth order state (i.e.,  $k = 0$ ), as indicated by  $\delta(k)$  in the equation.

Example MATLAB fitting code containing the Bloch-McConnell model with EPG implementation is provided at the following link: [https://github.com/rcsri/pulsed\\_saturation\\_epg](https://github.com/rcsri/pulsed_saturation_epg).